Materials Today Advances 32 (2026) 101018

Contents lists available at ScienceDirect

Materials Today Advances

journal homepage: www.journals.elsevier.com/materials-today-advances/

Wide-gap electronic structure, UV optical response and thermoelectric transport in lead-free Cs_2KGaCl_6 double perovskite

Zina Saoudi [a,b,*], M.A. Ghebouli [c,d], M. Fatmi [c], Murat Yaylacı [e,f,g], Elkenany Brens Elkenany [b,h], Rashed Abu Hammour [i], Ramzi Dhahri [b,h], Giovanni Neri [j,k]

[a] Department of Mathematics, College of Science and Arts, Najran University, Najran, Saudi Arabia
[b] Science and Engineering Research Center, Najran University, Najran, Saudi Arabia
[c] Research Unit on Emerging Materials (RUEM), University Ferhat Abbas of Setif 1, Setif, 19000, Algeria
[d] Department of Chemistry, Faculty of Sciences, University of M'sila University Pole, Road Bourdj Bou Arreiridj, M'sila, 28000, Algeria
[e] Department of Civil Engineering, Recep Tayyip Erdogan University, Rize, 53100, Türkiye
[f] Dijitalpark Teknokent, Murat Yaylacı-Luzeri R&D Engineering Company, Rize, 53100, Türkiye
[g] Turgut Kıran Maritime Faculty, Recep Tayyip Erdogan University, Rize, 53900, Türkiye
[h] Department of Physics, College of Science and Arts, Najran University, Najran, Saudi Arabia
[i] Faculty of Technical Education, Hourani Center for Applied Scientific Research (HCASR), Al-Ahliyya Amman University, Amman, Jordan
[j] Department of Engineering, University of Messina, Messina, 98166, Italy
[k] University of Turin University of Turin School of Medicine, Turin, Italy

ARTICLE INFO

Keywords:
Cs_2KGaCl_6
Lead-free double perovskite
FP-LAPW
WIEN2k
TB-mBJ
Spin–orbit coupling
Optical properties
Thermoelectric transport

ABSTRACT

Cubic Cs_2KGaCl_6 is investigated as a lead-free wide-gap double perovskite using an all-electron FP-LAPW WIEN2k framework that combines structural optimization, corrected electronic structure, optical response, semiclassical transport and finite-temperature lattice thermodynamics. The equilibrium volume increases from 2007.01 $bohr^3$ in LDA to 2246.55 $bohr^3$ in GGA-PBE, while the bulk modulus decreases from 32.71 to 23.98 GPa, confirming a comparatively soft chloride lattice. Cs_2KGaCl_6 is a direct-gap semiconductor at the scalar-relativistic level: the GGA-PBE gap of 3.033 eV increases to 4.905 eV with TB-mBJ. The corresponding electron/hole effective masses are 0.598/2.293 m_0 and 1.063/3.461 m_0, respectively, evidencing pronounced carrier asymmetry. TB-mBJ also reduces the static dielectric constant from 2.850 to 2.291 and the refractive index from 1.688 to 1.514, consistent with the widened gap. At 300 K, the maximum calculated power factor reaches 1.625 mW m^{-1} K^{-2} on the p-type side and 1.225 mW m^{-1} K^{-2} on the n-type side. The Slack-derived lattice thermal conductivity decreases with temperature and is treated as a screening estimate. An independent TB-mBJ + SOC reconstruction gives a direct Γ→Γ gap of 4.881 eV. A 2 × 2 × 2 finite-displacement phonon calculation shows no imaginary branches, while the final dense-k elastic constants satisfy the cubic Born criteria, providing complementary dynamical and mechanical stability checks.

1. Introduction

Lead-free $A_2BB'X_6$ double perovskites have attracted sustained interest because their ordered cation sublattice permits extensive electronic and structural tuning while avoiding Pb. Ghosh, Shankar and Kar reviewed the rapid development of this class and identified optoelectronics as a major application domain [1]. Recent work has moved beyond isolated electronic-structure calculations. $Cs_2SnGeCl_6$ was evaluated through a combined DFT and SCAPS-1D strategy that linked atomistic predictions to photovoltaic-device behavior [2]. Rb_2AlInX_6 compounds were investigated as lead-free energy-harvesting materials, illustrating the value of considering transport and electronic response together [3]. Multifunctional energy conversion has also been demonstrated theoretically in Rb_2BiAuX_6, where optoelectronic and thermoelectric properties were examined within the same chemical series [4]. At the nanoscale, lead-free double-perovskite nanocrystals have been surveyed with emphasis on structure, synthesis and optoelectronic applications [5]. Photocatalytic double halide perovskites form another branch of the field, with recent reviews emphasizing band-edge engineering for light-driven reactions [6]. Rb-based double halide

* Corresponding author. Department of Mathematics, College of Science and Arts, Najran University, Najran, Saudi Arabia.
E-mail address: zasaoudi@nu.edu.sa (Z. Saoudi).

https://doi.org/10.1016/j.mtadv.2026.101018
Received 27 August 2026; Received in revised form 9 October 2026; Accepted 10 October 2026
Available online 19 October 2026
2590-0498/© 2026 The Authors. Published by Elsevier Ltd. This is an open access article under the CC BY-NC license (http://creativecommons.org/licenses/by-nc/4.0/).

perovskites have additionally been assessed for photovoltaics, photocatalytic water splitting and CO_2 reduction [7]. The larger lead-free perovskite literature confirms the strategic importance of replacing Pb while preserving electronic tunability [8]. For Cs_2KGaCl_6, the most relevant chemical analogues are Ga-based double perovskites. Cs_2NaGaX_6 calculations demonstrate a pronounced halogen dependence of the lattice and optical gap [9]. Rb_2NaGaZ_6 provides another Ga-centered halide platform with energy-harvesting characteristics [10]. HSE06 calculations on $Cs_2TlGaCl_6$ and $Cs_2TlGaBr_6$ further show that Ga-containing double perovskites can sustain photovoltaic-relevant electronic structures [11]. The broader possibility of narrowing lead-free double-perovskite gaps has been demonstrated in $Cs_2AgBiBr_6$ [12]. Before detailed electronic analysis, structural feasibility must be considered. The tolerance factor proposed by Bartel et al. provides a modern descriptor for stability screening in both oxide and halide perovskites [13]. The present ground-state calculations adopt the PBE generalized-gradient approximation as the principal semilocal functional [14]. The wide-gap chloride regime makes band-gap correction especially important. The Tran-Blaha mBJ potential was developed to improve semiconductor and insulator gaps without the computational cost of hybrid functionals [15]. Its strengths and limitations were subsequently quantified by Tran and Blaha [16]. Improvements to the mBJ form were proposed by Koller, Tran and Blaha [17], and a systematic band-gap assessment was later reported by Jiang [18]. Spin-orbit coupling is evaluated as a separate relativistic contribution. Early work on halide perovskites established that SOC can significantly modify band-edge energies [19]. More recent calculations have highlighted the combined influence of symmetry breaking and SOC on the band gap, supporting explicit verification rather than assuming a negligible relativistic effect [20]. The numerical calculations use the full-potential LAPW methodology originally formulated for crystalline systems by Blaha and co-workers [21]. This formalism is implemented in WIEN2k through an APW + lo all-electron basis suitable for accurate total-energy and band calculations [22].

Finite-temperature thermodynamics are obtained from the static energy-volume data. Blanco, Francisco and Luaña introduced the GIBBS quasi-harmonic Debye framework for this purpose [23]. Otero-de-la-Roza and Luaña subsequently developed Gibbs2 with a more robust treatment of the static equation-of-state data [24]. The companion Gibbs2 work extended the available solid-state thermodynamic models [25]. Thermal conductivity is treated only as a screening quantity. Toher et al. showed how Debye temperature and Grüneisen parameter can be combined for high-throughput estimation of lattice thermal conductivity trends [26]. The electronic transport sector is evaluated with BoltzTraP [27] and its modern BoltzTraP2 extension [28]. The equation-of-state discussion follows established finite-strain and compressibility formalisms. Birch introduced the finite-elastic-strain description of cubic crystals [29], while Murnaghan provided a widely used pressure-volume equation of state for compressed media [30]. Recent first-principles studies provide a direct comparative basis for discussing the present compound. Na_2AgSbX_6 (X = Cl, F) was shown to possess tunable optoelectronic and thermoelectric properties [31]. Rb_2AgSbX_6 (X = Br, I) was subsequently examined for optical and plasmonic response [32]. K_2AgSbX_6 (X = Cl, F, I) established a direct connection between halogen-dependent band-gap engineering and thermoelectric performance [33]. Cs_2AgBiX_6 (X = Br, Cl) added a non-toxic Bi-based comparison spanning structural, electronic and thermoelectric behavior [34]. Multifunctional optoelectronic/thermoelectric response has also been reported for $Rb_2AsAuBr_6$ and $Rb_2AsAuCl_6$ [35]. Doping of $K_2AgSbBr_6$ by Cu^+, Bi^{3+} and I^- demonstrated strong control of the electronic and optical spectrum [36]. In-based $Cs_2InAgBr_6$ and $Cs_2InAgCl_6$ provide a further benchmark for wide-gap double perovskites with photovoltaic and thermoelectric potential [37].

Within this context, Cs_2KGaCl_6 represents a compact Ga/Cl member whose wide-gap electronic structure, low-frequency dielectric screening, carrier asymmetry and lattice heat transport require a dedicated all-electron analysis. The novelty of this work is an integrated assessment in which structural softness, band-gap correction, carrier-mass asymmetry, dielectric screening, optical losses, thermoelectric transport and lattice heat conduction are treated within one all-electron framework. A directly relevant study by Singh et al. examined the Cs_2KGaX_6 (X = Cl, Br, I) series using WIEN2k and Boltzmann transport and reported a 4.938 eV gap for Cs_2KGaCl_6 [38]. The close agreement with the present TB-mBJ value (4.905 eV) provides an external same-composition benchmark. Recent A_2AuSbZ_6 and Cs_2SeCl_6 calculations provide additional structural, electronic, optical and transport comparisons [39,40], while high-entropy $Cs_2AgInCl_6$ illustrates composition-driven tuning in lead-free chloride double perovskites [41]. Of more direct relevance to Ga-halide mechanics, Cs_2NaGaX_6 calculations show that halogen coordination strongly modifies elastic response and failure behavior [42]. The literature discussion also includes to Cs_2MZ_6 (M = Ti, Zr, Hf; Z = Cl, I) [43], $CsTmX_3$ (X = F, Cl, Br, I) [44], and Rb_2MgSnY_6 (Y = I, Br, Cl) [45], which collectively document strong halide control of band gaps, optical response, thermodynamics and transport. For the mechanical and structural discussion, the Rb_3SbX_6 family [46], Ga-based $A_2LiGaBr_6$ (A = Na, K) [47], $K_2Pt(Cl/Br)_6$ [48], and K_2InLiX_6 [49] provide complementary benchmarks for elastic anisotropy, phonon stability, optical response and, where reported, thermoelectric behavior. These studies offer complementary reference points for the present analysis. An integrated description of Cs_2KGaCl_6 requires the electronic band edges, lattice stability and finite-temperature transport to be considered within a consistent computational framework. In particular, the connection between relativistic band-edge shifts, carrier asymmetry and quasi-harmonic lattice response is important for assessing the physical limits of thermoelectric screening predictions. The present work examines these properties through all-electron electronic-structure calculations, harmonic phonons, elastic analysis and temperature-dependent Debye–Grüneisen modeling.

2. Computational methodology

All ground-state calculations were carried out with the all-electron full-potential linearized augmented-plane-wave plus local-orbital method implemented in WIEN2k [21,22]. The crystal volume is divided into non-overlapping muffin-tin spheres and an interstitial region. Inside each sphere, radial solutions multiplied by spherical harmonics describe the wave functions; plane waves span the interstitial space, while local orbitals improve the representation of semi core and valence states. The cubic elpasolite-type structure was used as the starting model. WIEN2k initialization included symmetry generation, nearest-neighbour analysis, muffin-tin-radius consistency, construction of atomic starting densities, k-mesh generation and assembly of the initial crystalline charge density. Basis quality was controlled through RMTKmax, and Brillouin-zone convergence was tested independently before production runs. The convergence workflow retained RMTKmax = 7 and a dense production k mesh corresponding to the converged 1000-point request in the full Brillouin zone. Self-consistency was pursued until the total-energy variation was below 1×10^{-4} Ry. Within the WIEN2k cycle, LAPW0 updates the effective potential, LAPW1 solves the valence eigenproblem, LAPW2 constructs the valence density, core states are treated separately and the total density is mixed until convergence. The production electronic structures used muffin-tin radii RMT(Cs) = 2.50, RMT(K) = 2.50, RMT(Ga) = 2.40 and RMT (Cl) = 2.17 bohr, with RMTKmax = 7.The optimized phase is cubic Fm-3m (No. 225). The conventional Wyckoff assignment is Cs: 8c, K: 4a, Ga: 4b and Cl: 24e. From the GGA equilibrium primitive-cell volume of 2246.551 $bohr^3$, the corresponding conventional cubic lattice constant is $a_0 = 10.997$ Å. These crystallographic descriptors are stated explicitly to separate structural identification from subsequent stability tests. Structural properties were evaluated using both LDA and GGA-PBE [14].

A series of compressed and expanded volumes was calculated while preserving cubic symmetry, and the resulting E(V) data were fitted with a third-order Birch–Murnaghan equation of state [29]. The fit yields the equilibrium volume V_0, bulk modulus B_0, pressure derivative B' and minimum energy E_0. Electronic bands and densities of states were first computed with GGA-PBE. The Tran–Blaha modified Becke–Johnson potential was subsequently applied to improve the band-gap description [15–18]. Spin–orbit coupling was then introduced in the second-variational framework available in WIEN2k. The same high-symmetry path was used wherever possible so that changes in the band edges could be compared directly. Directional electron and hole masses were estimated from local parabolic fits around the conduction- and valence-band extrema. Only fits judged sufficiently reliable were retained for interpretation; the masses are therefore treated as local curvature descriptors rather than complete three-dimensional mobility tensors. The optical response was obtained from the complex dielectric function $\varepsilon(\omega) = \varepsilon_1(\omega) + i\varepsilon_2(\omega)$. Interband matrix elements determine ε_2, while ε_1 follows from the Kramers–Kronig relationship. Absorption coefficient, refractive index, extinction coefficient, reflectivity, optical conductivity and the electron energy-loss function were derived from the same dielectric dataset. Semiclassical transport was evaluated from the WIEN2k eigenvalues using a BoltzTraP/BoltzTraP2-type interpolation [27,28]. Seebeck coefficient, electrical conductivity and electronic thermal conductivity were calculated versus chemical potential at 300, 600 and 900 K. A fixed relaxation time of 10^{-14} s was used when converting σ/τ and $\kappa e/\tau$ into plotted σ and κe and when evaluating the power factor. The value $\tau = 10^{-14}$ s is used only as a representative conversion factor. The primary band-structure outputs are σ/τ and $\kappa e/\tau$. Because σ, κe and PF scale with τ in the CRTA, values inferred for $\tau = 10^{-15}$, 10^{-14} and 10^{-13} s differ by the corresponding decade factors, whereas S is τ-independent. Absolute conductivity-related values and the resulting ZT are therefore screening-level quantities rather than intrinsic material constants. The optical spectra are interpreted within the independent-particle interband picture used by the WIEN2k optical module. The same converged production k-point framework and a common spectral window were used for the PBE, TB-mBJ and verified TB-mBJ + SOC comparisons. Local-field and explicit electron–hole (excitonic) interactions are not included; consequently, the calculated electronic gap, independent-particle optical onset and an experimental excitonic optical gap should not be regarded as identical quantities. Cs_2KGaCl_6 contains nominally closed-shell Cs^+, K^+, Ga^{3+} and Cl^- ions and no open-shell transition-metal magnetic sublattice. The electronic calculations are therefore treated as nonmagnetic. Introducing arbitrary FM/AFM order or Jahn–Teller spin-state arguments would not be physically motivated for this closed-shell composition. For the final SOC verification, the converged TB-mBJ charge density was retained and SOC was applied in the WIEN2k second-variational step. The Fermi level and band indices were checked directly against the post-SOC eigenvalues. The resulting VBM and CBM both occur at Γ, giving a direct gap of 4.881 eV; the earlier near-zero automated value was traced to post-processing band-index misassignment and is not used. Finite-temperature lattice properties were obtained from the GGA E(V) surface using quasi-harmonic Debye/GIBBS concepts [23–26]. Bulk modulus, Cp, Cv, Debye temperature, equilibrium volume, Grüneisen parameter and thermal expansion were followed with temperature. The Slack model supplied a screening $\kappa L(T)$; because it does not contain explicit phonon lifetimes, the absolute κL and any ZT derived from it are discussed conservatively. The quasi-harmonic Debye/Slack treatment is a model built from the static E(V) surface and does not include mode-resolved phonon lifetimes, explicit high-order anharmonicity, structural transformations, decomposition or melting. Predictions approaching 1000 K are consequently interpreted as trends within the assumed cubic phase. The newly calculated harmonic phonon spectrum is used only to assess dynamical stability and is not substituted for a full anharmonic thermal-conductivity calculation. Because semilocal PBE-GGA generally underestimates semiconductor band gaps owing to the approximate exchange-correlation treatment and missing derivative discontinuity, TB-mBJ was used here as the principal gap-corrected semilocal potential. Harmonic phonons were evaluated with the finite-displacement method using PHONOPY interfaced with WIEN2k forces for a $2 \times 2 \times 2$ supercell; the resulting force constants were used to construct the phonon dispersion and phonon DOS. For the Debye–-Grüneisen analysis, the primitive Cs_2KGaCl_6 formula unit contains ten atoms (2 Cs, 1 K, 1 Ga and 6 Cl). Accordingly, the GIBBS2 input uses vfree = 10 and a formula-unit mass of 587.33220392 u. Temperature-dependent equilibrium volumes, Debye temperatures and Grüneisen parameters were extracted from the resulting quasi-harmonic calculation. The Slack treatment is regarded as a model-based estimate rather than a mode-resolved prediction of lattice thermal conductivity.

3. Results and discussion

The optimized cubic crystal structure of Cs_2KGaCl_6 is shown in Fig. 1. The framework consists of alternating KCl_6 and $GaCl_6$ octahedra, while Cs occupies the cavities of the double-perovskite lattice.

3.1. Numerical convergence and equation of state

Fig. 2 combines the basis/k-point convergence diagnostics with the LDA and GGA-PBE equations of state. The numerical tests are shown before the structural fit because the energy scale defining the equilibrium minimum is meaningful only after the total energy becomes insensitive to the computational controls. The corresponding Birch–Murnaghan equation-of-state parameters are summarized in Table 1.

The fitted minima show a clear LDA–GGA contrast. GGA-PBE expands the equilibrium volume by 11.9% relative to LDA and lowers the bulk modulus from 32.71 to 23.98 GPa. The broader GGA minimum therefore represents a more compliant lattice, whereas the tighter LDA basin reflects stronger effective binding. Because both minima are bracketed by calculated points, the structural parameters are obtained from interpolation rather than edge extrapolation. The broader GGA minimum indicates hydrostatic compliance but is not, by itself, a dynamical-stability criterion.A useful structural comparison is provided by lead-free Cs_2AgBiX_6 (X = Br, Cl), for which first-principles calculations jointly linked equilibrium structural descriptors with electronic and thermoelectric behavior. That comparison reinforces the need to interpret the relatively low bulk modulus of Cs_2KGaCl_6 as a measure of hydrostatic compliance rather than as a stand-alone proof of lattice stability [34].

3.2. Electronic structure and SOC sensitivity

Fig. 3 is organized by electronic-structure level so that each band dispersion can be read next to its corresponding density of states. This layout allows the gap correction, band curvature and redistribution of spectral weight to be followed consistently from GGA-PBE to TB-mBJ and SOC.

The scalar-relativistic calculations describe a direct wide-gap semiconductor: Eg changes from 3.033 eV in GGA-PBE to 4.905 eV with TB-mBJ. Independent reconstruction of the SOC eigenvalues confirms that the VBM and CBM remain at Γ and gives a direct TB-mBJ + SOC gap of 4.881 eV. Thus, SOC lowers the TB-mBJ gap by only about 0.0245 eV; the earlier automated near-zero value was a band-indexing artifact and is removed from the physical interpretation. The verified band plots and DOS in Fig. 3 use a common Fermi-level alignment. The 4.905 eV TB-mBJ gap is also consistent with the 4.938 eV value reported for Cs_2KGaCl_6 by Singh et al. [38]. This agreement concerns the fundamental one-electron electronic gap. It should not be equated directly with an excitonic optical gap, since the present independent-particle optical treatment does not include explicit electron–hole binding.The DOS should be read together with the dispersion rather than as an

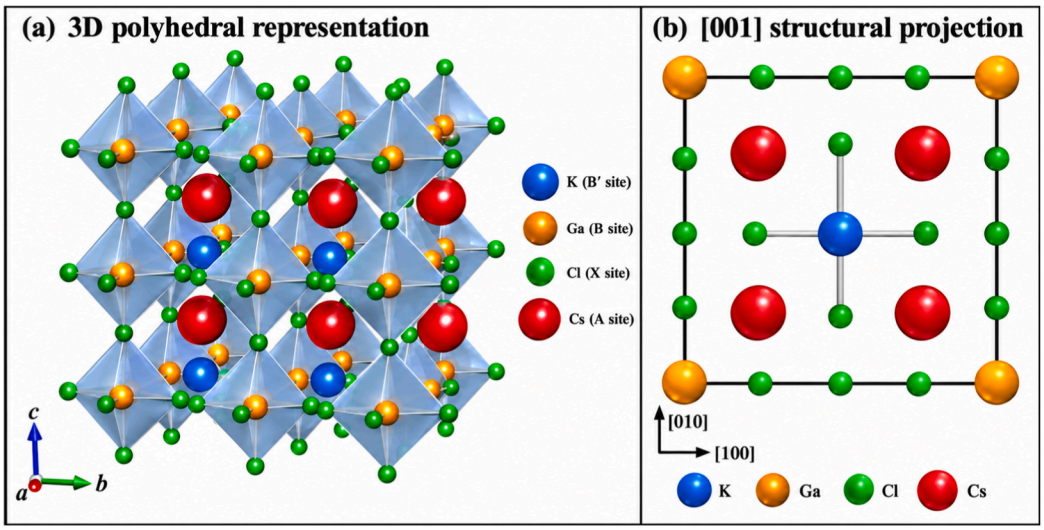


Fig. 1. Crystal structure of cubic Cs_2KGaCl_6 shown as (a) a three-dimensional view of the ordered double-perovskite framework and (b) a [001] projection with distinct colors for Cs, K, Ga and Cl. The combined representation presents complementary 3D and 2D structural visualizations.

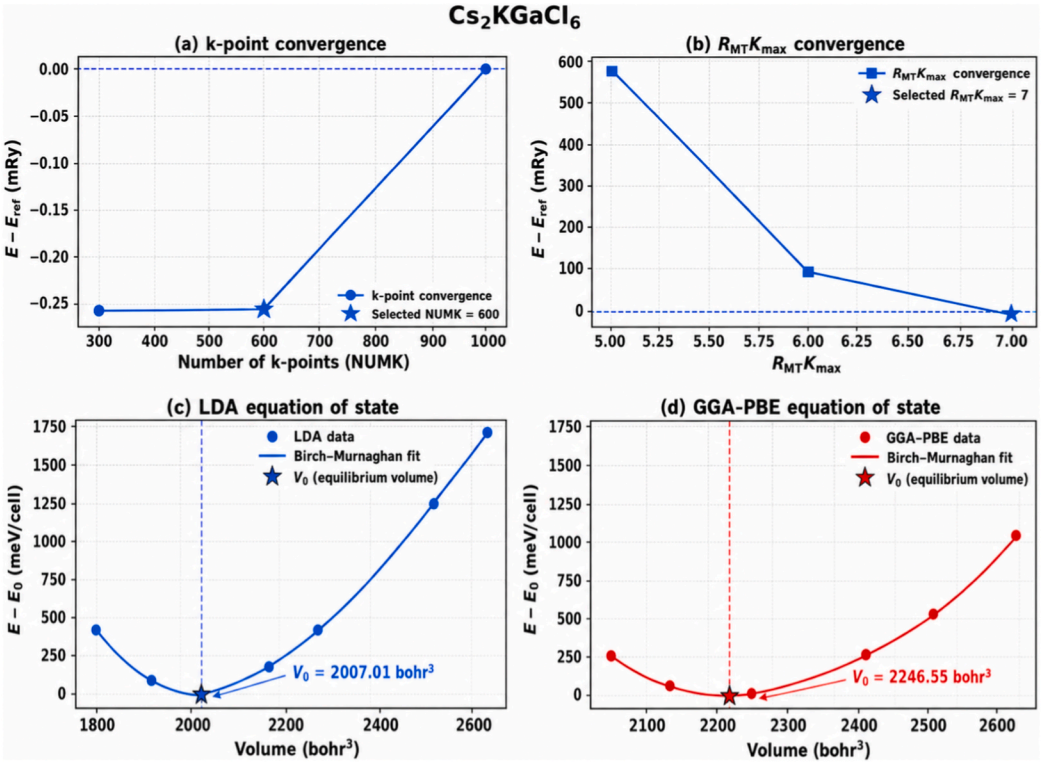


Fig. 2. Numerical convergence and equation of state of Cs_2KGaCl_6. Upper block: k-point and RMTKmax convergence tests. Lower block: LDA and GGA-PBE total-energy–volume curves and their equilibrium minima.

Table 1
Birch–Murnaghan equation-of-state parameters of Cs_2KGaCl_6.

Method	V_0 (bohr^3)	B_0 (GPa)	B′	E_0 (Ry)
LDA	2007.0140	32.7069	5.0358	−41744.2652
GGA	2246.5510	23.9837	4.3418	−41792.8668

independent spectrum. A steep, dispersive band edge produces a different near-edge state accumulation from a flat band, and the effective-mass values quantify this contrast. The increase of m*e from 0.598 to 1.063 m_0 and of m*h from 2.293 to 3.461 m_0 after TB-mBJ shows that the corrected potential changes not only the gap but also the local curvature. The hole/electron mass ratio remains large, about 3.8 in GGA and 3.3 in TB-mBJ, providing a robust electronic basis for the asymmetric p- and n-type transport response.Composition-driven band-gap engineering is also well established in related lead-free double perovskites. In K_2AgSbX_6 (X = Cl, F, I), halide substitution produces pronounced changes in the electronic gap, SOC response and thermoelectric behavior [33], whereas Cu^+, Bi^{3+} and I^- substitutions in $K_2AgSbBr_6$ shift the band edges and optical window in different directions [36]. These comparisons support the present interpretation that the corrected gap and near-edge dispersion of Cs_2KGaCl_6 are sensitive to

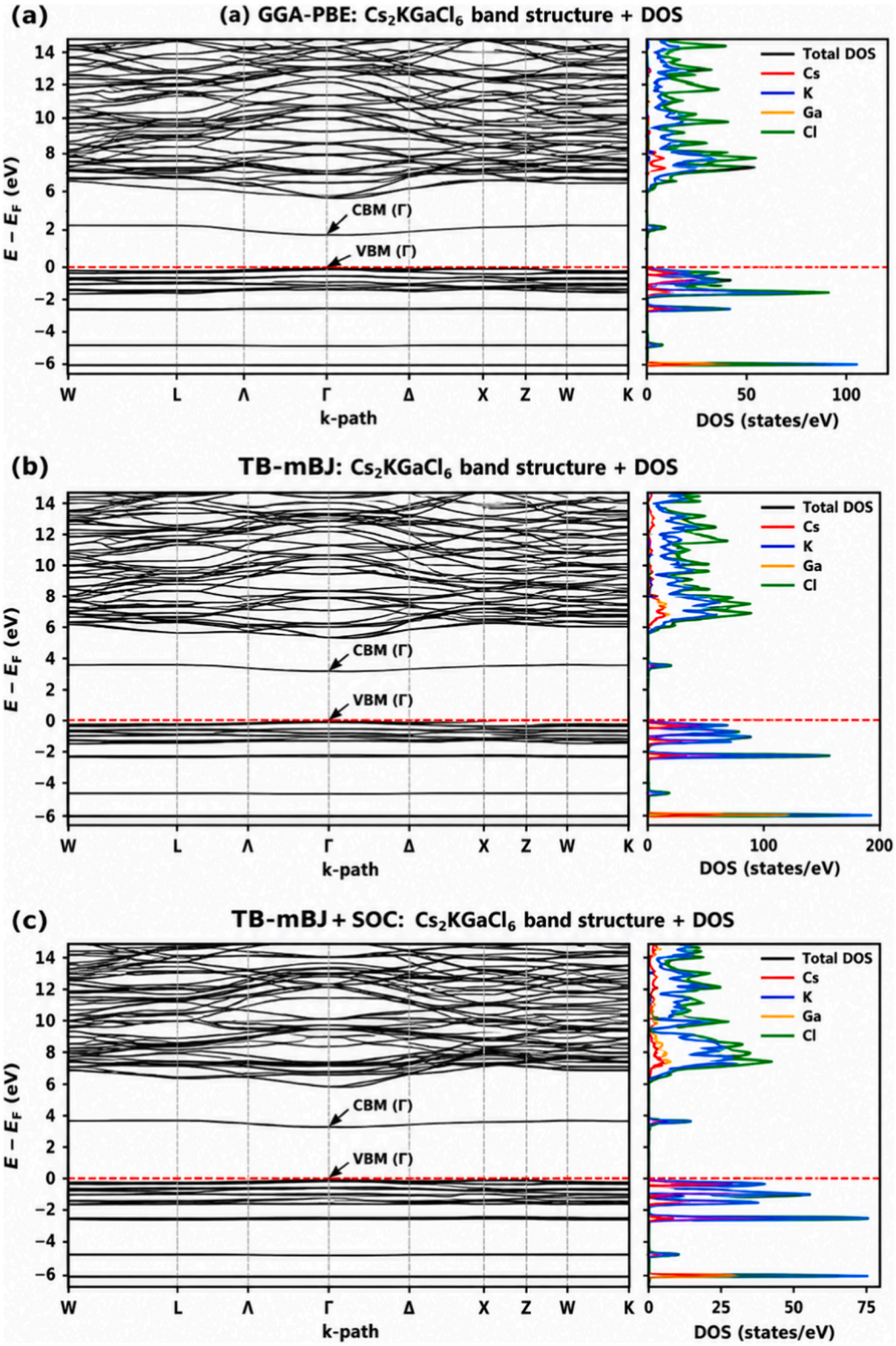


Fig. 3. Band structure and atom-resolved density of states of Cs_2KGaCl_6: (a) GGA-PBE, (b) TB-mBJ and (c) independently verified TB-mBJ + SOC. The VBM and CBM are explicitly identified at Γ.

the detailed chemical potential and orbital environment rather than to a rigid energy shift alone.The magnetic character of halide double perovskites is strongly chemistry dependent. V-containing K_2CuVCl_6 and Rb_2CuVCl_6 were predicted to be half-metallic ferromagnets because exchange-split V-3d states dominate the states around the Fermi level [50]. Cs_2KGaCl_6 is fundamentally different: the nominal Cs^+, K^+, Ga^{3+} and Cl^- ions do not form an open-shell transition-metal magnetic sublattice. The electronic and static optical parameters are summarized in Table 2.

Accordingly, an arbitrary FM/AFM energy comparison or a Jahn-Teller interpretation is not physically motivated for the present closed-shell compound. For a quantitative comparison, Table 3 benchmarks

Table 2
Electronic gap, band-edge, representative effective-mass and static optical parameters of Cs_2KGaCl_6.

Method	Gap (eV)	Type	VBM k-point	CBM k-point	m^*_e/m_0	m^*_h/m_0	$\varepsilon_1(0)$	n(0)
GGA-PBE	3.03316	Direct	Γ	Γ	0.598	2.293	2.850	1.688
TB-mBJ	4.90512	Direct	Γ	Γ	1.063	3.461	2.291	1.514
TB-mBJ + SOC	4.88061	Direct	Γ	Γ	≈1.00	5.703 (Γ–L)	2.289	1.513

Table 3
Quantitative benchmark of Cs_2KGaCl_6 against closely related halide perovskites. NR = not numerically reported in the accessible source used for comparison.

Material	a_0 (Å)	B_0 (GPa)	Eg (eV)	Elastic/dynamical benchmark	Optical/thermoelectric benchmark	Ref.
Cs_2KGaCl_6 (this work)	10.997	23.98	4.905 TB-mBJ; 4.881 +SOC	C_{11} = 18.546, C_{12} = 18.539, C_{44} = 19.998 GPa; no imaginary phonons	n(0) = 1.514 (TB-mBJ); PFmax = 1.625 mW m^{-1} K^{-2} at 300 K (p-type, $\tau = 10^{-14}$ s)	Present
Cs_2KGaCl_6	NR	NR	4.938	E(V) structural stability reported	Optical response and Boltzmann transport (S, σ, κ) reported	[38]
$Rb_2MgSnCl_6$	10.97	24.33	2.45	Stable; anisotropic and ductile; positive phonon frequencies	High optical conductivity, low reflectivity, strong absorption	[45]
Rb_3SbCl_6	NR	19.03	NR	C_{11} = 46.29, C_{12} = 5.40, C_{44} = 3.46 GPa; Y_H = 20.41 GPa; ν_H = 0.32	UV/visible optical response analyzed; thermodynamic stability reported	[46]
$Na_2LiGaBr_6$	NR	NR	1.42	Mechanically and dynamically stable; no imaginary phonons	Photovoltaic-oriented optical response reported	[47]
$K_2LiGaBr_6$	NR	NR	1.29	Mechanically and dynamically stable; no imaginary phonons	Photovoltaic-oriented optical response reported	[47]
K_2PtCl_6	NR	NR	2.60	Anisotropic/ductile; positive phonon frequencies	Room-temperature ZT ≈ 0.68	[48]
K_2InLiX_6 (X = Cl,Br,I)	increases Cl→I	NR	direct; halide-dependent	Elastic, thermodynamic and dynamical stability; positive phonons	Strong absorption/high conductivity/low reflectivity; Br/I highlighted for solar cells	[49]

the present structural, electronic, elastic, optical and thermoelectric descriptors against the closest available halide-perovskite literature; entries are reported only when the cited source provides the corresponding quantity.

Table 3 highlights the distinctive position of Cs_2KGaCl_6 among related halide perovskites. Its lattice parameter (10.997 Å) and bulk modulus (23.98 GPa) agree closely with comparable halide systems [45], whereas its direct TB-mBJ band gap of 4.905 eV (4.881 eV with SOC) is considerably larger than those reported for several related compounds [45,47,48]. Together with the absence of imaginary phonon modes, n(0) = 1.514, and a maximum power factor of 1.625 mW m^{-1} K^{-2} at 300 K, these results establish Cs_2KGaCl_6 as a dynamically stable wide-gap material with complementary optical and thermoelectric characteristics. The comparison with related halide series [49] further demonstrates the important role of halogen chemistry in tuning these properties.

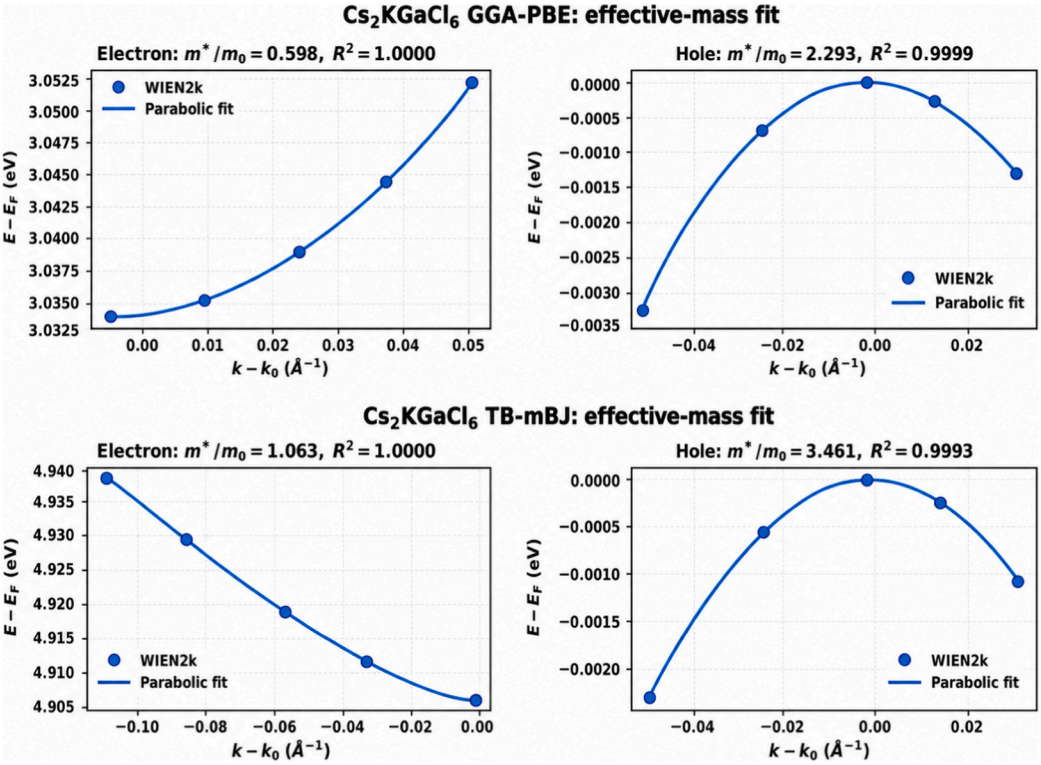


Fig. 4. Local parabolic effective-mass fits for Cs_2KGaCl_6: (a) GGA-PBE and (b) TB-mBJ.

3.3. Effective masses and carrier asymmetry

Fig. 4 isolates the two reliable scalar-relativistic parabolic fits used to quantify band-edge curvature. Keeping the GGA-PBE and TB-mBJ fits together makes it possible to see whether the band-gap correction also changes the local transport curvature.

The GGA electron mass is 0.598 m_0, compared with 2.293 m_0 for holes; TB-mBJ changes these values to 1.063 and 3.461 m_0. These are local directional curvature descriptors, not mobility values. The fitting window was tested locally around the band extrema rather than inferred from the full high-symmetry path. For the independently verified SOC result, ultradense sampling around Γ gives electron masses of about 1.003 m_0 along Γ–X and 0.991 m_0 along Γ–L. The SOC-split valence edge is non-parabolic along Γ–X, so no artificial single hole mass is assigned there; a robust Γ–L heavy-hole fit gives 5.703 m_0 ($R^2 \approx 0.9975$). The heavier holes and lighter electrons indicate different band curvatures, but any statement about mobility remains conditional on comparable scattering rates and relaxation times.

The simultaneous gap widening and curvature change under TB-mBJ therefore cannot be described as a rigid scissor shift. It reflects the changed semilocal potential and the resulting redistribution of near-edge hybridization/dispersion. The calculated masses quantify band curvature only; they do not, by themselves, establish a carrier mobility without a scattering model. For quantitative photovoltaic context, a recent review reports m*e/m_0 and m*h/m_0 values of 0.19/0.25 for $MAPbI_3$, 0.37/0.14 for $Cs_2AgBiBr_6$ and 1.06/0.59 for Si [51]. Thus, the present PBE electron mass (0.598 m_0) is heavier than $MAPbI_3$ and $Cs_2AgBiBr_6$ but lighter than the corresponding Si density-of-states value, whereas the TB-mBJ/SOC electron masses (≈1.0–1.06 m_0) approach that Si benchmark. In contrast, the calculated hole effective masses (2.293–5.703 m_0) exceed the corresponding previously reported values [31,35,37]. The physically meaningful conclusion is therefore a pronounced electron–hole curvature asymmetry, not a claim of intrinsically high mobility; n-type transport may be favored only if comparable scattering times are assumed.

3.4. Optical response

Fig. 5 condenses the principal optical functions into absorption, ε_1, ε_2 and reflectivity, while Fig. 6 adds refractive index and electron energy loss. The separation into two figures preserves readability without discarding any major optical observable.

The static response decreases when the electronic gap is corrected: $\varepsilon_1(0)$ changes from 2.850 to 2.291, while n(0) drops from 1.688 to 1.514. This is the expected signature of reduced low-energy polarizability in a wider-gap solid. The absorption onset shifts toward higher photon energy under TB-mBJ, and the ε_2 maxima mark clusters of allowed interband transitions rather than isolated single-band events. Reflectivity remains an important counterpoint to absorption because only the non-reflected fraction can contribute to internal optical excitation.

The refractive-index spectrum mirrors the dielectric dispersion and provides an independent check of the static response through $n(0) \approx \sqrt{\varepsilon_1(0)}$. At higher photon energies, oscillatory changes in n(ω) track resonant interband regions. The loss function is weak at low energy and develops stronger structures only after substantial electronic excitation becomes possible. These maxima are best described as collective/plasmon-like loss features unless a simultaneous dielectric zero crossing is demonstrated. The static optical constants provide a quantitative consistency test. The relation $n(0) \approx \sqrt{\varepsilon_1(0)}$ gives values fully compatible with the tabulated pairs 2.850/1.688 for GGA-PBE and 2.291/1.514 for TB-mBJ. The reduction of $\varepsilon_1(0)$ by about 20% and of n(0) by about 10% follows the widening of the electronic gap and indicates weaker low-frequency electronic screening. In practical terms, the TB-mBJ description predicts a less polarizable transparent regime before interband transitions become active. A loss-function maximum is described as plasmon-like only when it is accompanied by the dielectric-response condition Re[ε(ω)] approaching/crossing zero while Im[ε(ω)] remains comparatively small. Otherwise, it is treated simply as an interband/collective loss maximum. Application language is correspondingly restricted to potential UV/near-UV optical use rather than

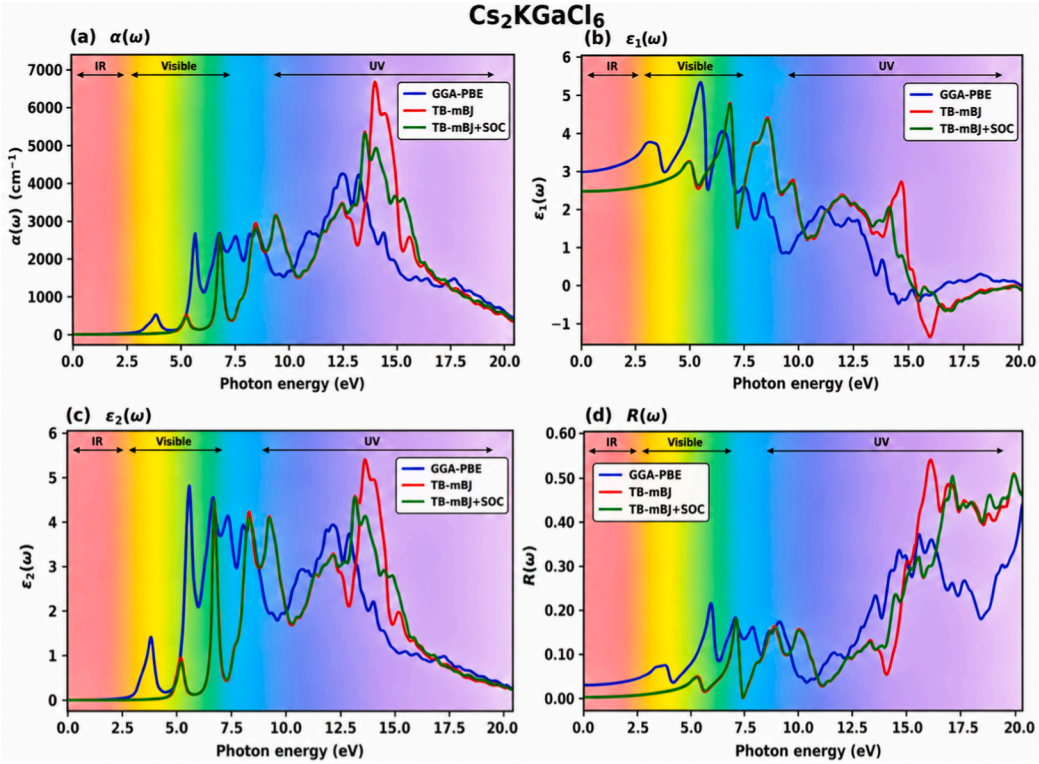


Fig. 5. Selected optical functions of Cs_2KGaCl_6: (a) absorption coefficient, (b) $\varepsilon_1(\omega)$, (c) $\varepsilon_2(\omega)$, and (d) reflectivity for GGA-PBE, TB-mBJ and TB-mBJ + SOC.

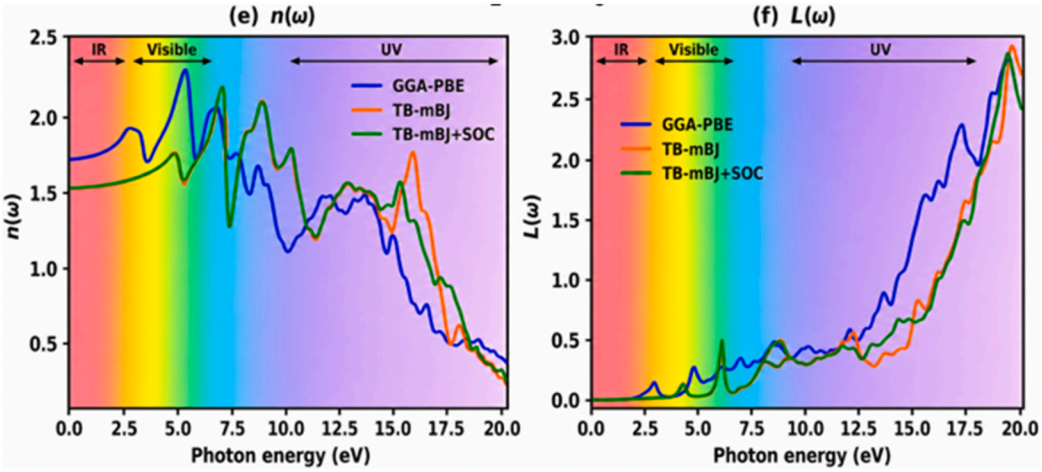


Fig. 6. Additional optical functions of Cs_2KGaCl_6: (a) refractive index n(ω) and (b) electron energy-loss function L(ω) for the three electronic-structure treatments.

demonstrated device functionality. For Cs_2KGaCl_6, the most important optical result is the TB-mBJ-driven shift of the absorption onset to higher energy together with the reduction of $\varepsilon_1(0)$ from 2.850 to 2.291 and n(0) from 1.688 to 1.514. The dominant loss structures lie well above the fundamental onset, supporting a UV/near-UV rather than low-energy metallic interpretation. This composition-specific behavior is consistent with the strong halide dependence reported in related perovskites [44–46].

3.5. *Thermoelectric transport under the constant-τ approximation*

Fig. 7 places the four central electronic transport observables on a common chemical-potential axis at 300, 600 and 900 K. The curves are interpreted together because optimizing S alone would not maximize the power factor, and increasing σ simultaneously raises the electronic heat-conduction channel. The transport parameters of Cs_2KGaCl_6 at the

Table 4
Transport parameters of Cs_2KGaCl_6 at the calculated power-factor maxima ($\tau = 10^{-14}$ s).

T (K)	Carrier	μPFmax (eV)	S (μV/K)	σ (S/m)	κe (W/mK)	PFmax (mW m^{-1} K^{-2})
300	p	−0.5809	−192.35	4.391e+04	0.115	1.625
300	n	0.0093	190.30	3.381e+04	0.082	1.225
600	p	−0.5896	−118.82	5.662e+04	0.606	0.799
600	n	0.0567	200.77	2.352e+04	0.051	0.948
900	p	−0.0036	90.07	4.532e+04	0.219	0.368
900	n	0.1084	203.82	1.793e+04	0.063	0.745

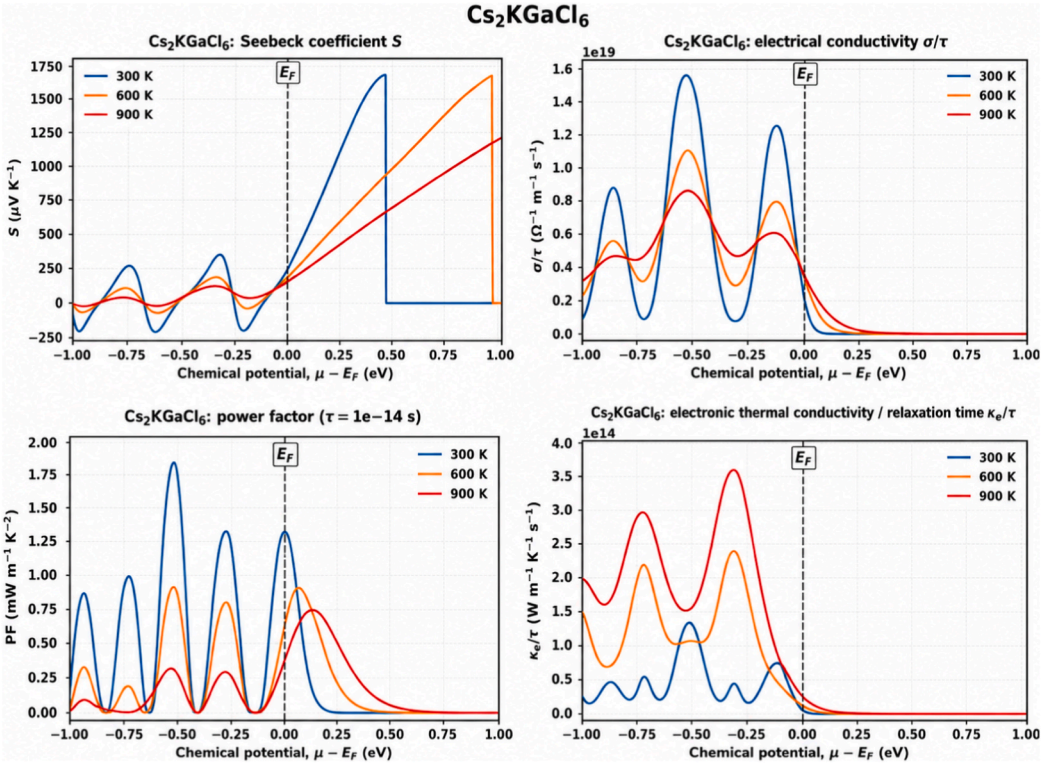


Fig. 7. Thermoelectric transport of Cs_2KGaCl_6 at 300, 600 and 900 K: (a) Seebeck coefficient, (b) electrical conductivity for $\tau = 10^{-14}$ s, (c) power factor, and (d) electronic thermal conductivity.

calculated power-factor maxima ($\tau = 10^{-14}$ s) presented in Table 4.

At 300 K, the p-side and n-side PF maxima are 1.625 and 1.225 mW m^{-1} K^{-2}, respectively. The corresponding Seebeck magnitudes are about 192.4 and 190.3 μV K^{-1}. As temperature rises, the optimal μ shifts and the peak PF decreases, especially on the p-type branch. This behavior shows that thermal broadening does not automatically improve performance: it can weaken the energy selectivity that supports large S. Because σ and κe both scale with the assumed τ, the most transferable comparison is the shape and location of the transport windows rather than their absolute magnitudes. Because τ is not calculated from first principles here, the absolute σ, κe and PF values should be read together with σ/τ and κe/τ. Changing τ from 10^{-14} s to 10^{-15} or 10^{-13} s rescales these quantities by factors of 0.1 and 10, respectively. The chemical-potential locations and the Seebeck trends are more transferable than the assumed-τ absolute magnitudes. A quantitative carrier-density conversion is not asserted because the archived μ-dependent dataset used for this manuscript does not contain a uniquely traceable absolute carrier-concentration output at every reported optimum.

To make the carrier optimization and lattice heat transport directly comparable, Fig. 8 combines the figure of merit ZT as a function of chemical potential with the Slack lattice thermal conductivity. Presenting these quantities side by side highlights both the preferred carrier-optimization windows and the phonon-limited heat-transport trend.

Fig. 8(a) shows a strongly non-monotonic ZT(μ) response. The very large high-temperature maxima arise from combining the constant-τ electronic transport model with an exceptionally small Slack-estimated lattice thermal conductivity. They are therefore theoretical screening indicators rather than predictions of experimentally achievable bulk ZT. The small low-μ structures are retained only as numerical features of the interpolation and are not used as performance claims. The wide-gap optical regime and the thermoelectric screening regime correspond to distinct carrier-density/doping conditions and should not be interpreted as simultaneous device functionalities. Fig. 8(b) reports the Slack-type lattice thermal conductivity κL(T), which decreases with temperature within the quasi-harmonic Debye/Slack model. Its high-temperature values approach the 10^{-3} W m^{-1} K^{-1} scale and should not be interpreted as quantitatively converged phonon-transport predictions because no mode-resolved lifetimes or third-order force constants are included. The Slack expression uses the average atomic mass, Debye temperature, Grüneisen parameter, volume per atom, number of atoms in the primitive cell and temperature; the temperature-dependent Debye/Grüneisen/volume trends are supplied by the quasi-harmonic model. The role of κL in ZT is consequently discussed as a sensitivity/screening input rather than an experimentally established thermal conductivity. Because κL is estimated within the Slack/Debye approximation, the absolute ZT magnitudes should be interpreted primarily as screening indicators. Nevertheless, the combined ZT–κL analysis clearly identifies improved high-temperature performance together with a pronounced preference for n-type optimization. Related first-principles studies further show that optoelectronic and thermoelectric functionality can coexist in lead-free double perovskites, but the balance depends strongly on chemistry and the thermal-transport model. Na_2AgSbX_6 (X = Cl, F) displays tunable optical gaps and thermoelectric response [31], $Rb_2AsAuBr_6/Rb_2AsAuCl_6$ combines optoelectronic absorption with sizable Seebeck response [35], and $Cs_2InAgBr_6/Cs_2InAgCl_6$ provides another benchmark linking structural, optical and thermoelectric properties [37]. These comparisons support treating the present Cs_2KGaCl_6 transport results as composition-specific screening trends rather than universal performance metrics.F or a quantitative assessment of lattice thermal conductivity, the numerical parameters entering the Slack model are summarized in Table 5 at representative temperatures. The maximum thermoelectric figure of merit (ZT) reaches approximately 7.61, 23.17, and 34.39 at 300, 600, and 900 K, respectively, assuming a constant relaxation time of 10^{-14} s. The lattice thermal conductivity is described within the Slack model using temperature-dependent Debye temperature, Grüneisen parameter, and equilibrium volume. These findings highlight the promising thermoelectric performance of Cs_2KGaCl_6 within the adopted theoretical framework.

The GIBBS2-derived parameters provide a temperature-resolved basis for examining lattice thermal response. Their evolution is consistent with thermal expansion, elastic softening and a progressive reduction in characteristic vibrational frequencies. The numerical inputs are given in Table 5, while the resulting Slack conductivity should be interpreted as a screening-level model quantity. The estimated lattice thermal conductivities are 0.014698, 0.005614 and 0.002564 W m^{-1} K^{-1} at 300, 600 and 900 K, respectively. The temperature-dependent structural and vibrational descriptors are summarized in Table 5. Between 300 and 900 K, the equilibrium volume increases from 2311.9017 to 2493.3932 $bohr^3$, while the Debye temperature decreases from 216.86 to 188.63 K and the Grüneisen parameter rises from 1.7393 to 1.9660. The mean atomic mass is 58.733 u/atom for the ten-atom formula unit. These trends reflect lattice expansion and increased anharmonic sensitivity with temperature. Quantitative thermal-conductivity and ZT estimates remain dependent on the chosen Slack implementation and electronic transport assumptions.

3.6. Quasi-harmonic thermodynamic trends

Fig. 9 summarizes the remaining quasi-harmonic thermodynamic descriptors used to interpret the finite-temperature response of the crystal.These temperature-dependent quantities complement the ZT/κL analysis by tracking elastic softening, heat-capacity saturation, volume expansion, and anharmonicity across the 0–1000 K interval.

The six thermodynamic curves form a consistent finite-temperature picture. Equilibrium volume expands while the bulk modulus softens,

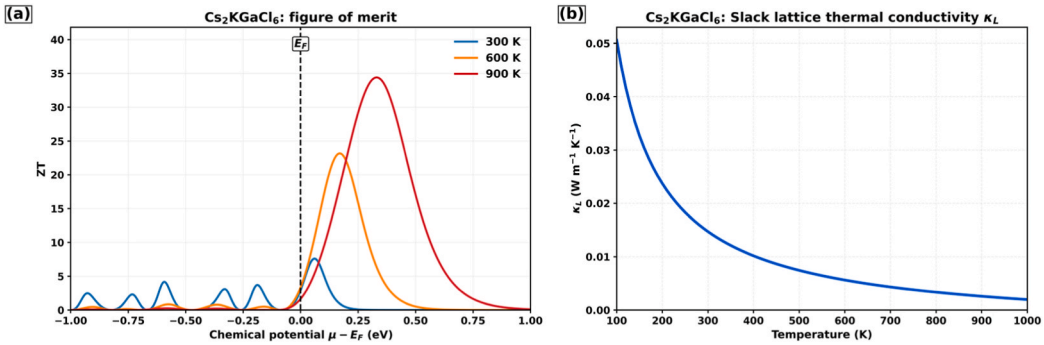


Fig. 8. (a) Thermoelectric figure of merit ZT of Cs_2KGaCl_6 as a function of chemical potential at 300, 600 and 900 K. The dashed vertical line marks the Fermi level, μ − EF = 0 eV. (b) Temperature dependence of the Slack-type lattice thermal conductivity, κL, of Cs_2KGaCl_6 from 100 to 1000 K. The lattice-conductivity curve uses the temperature-dependent quasi-harmonic descriptors and the Slack-model scaling approximation.

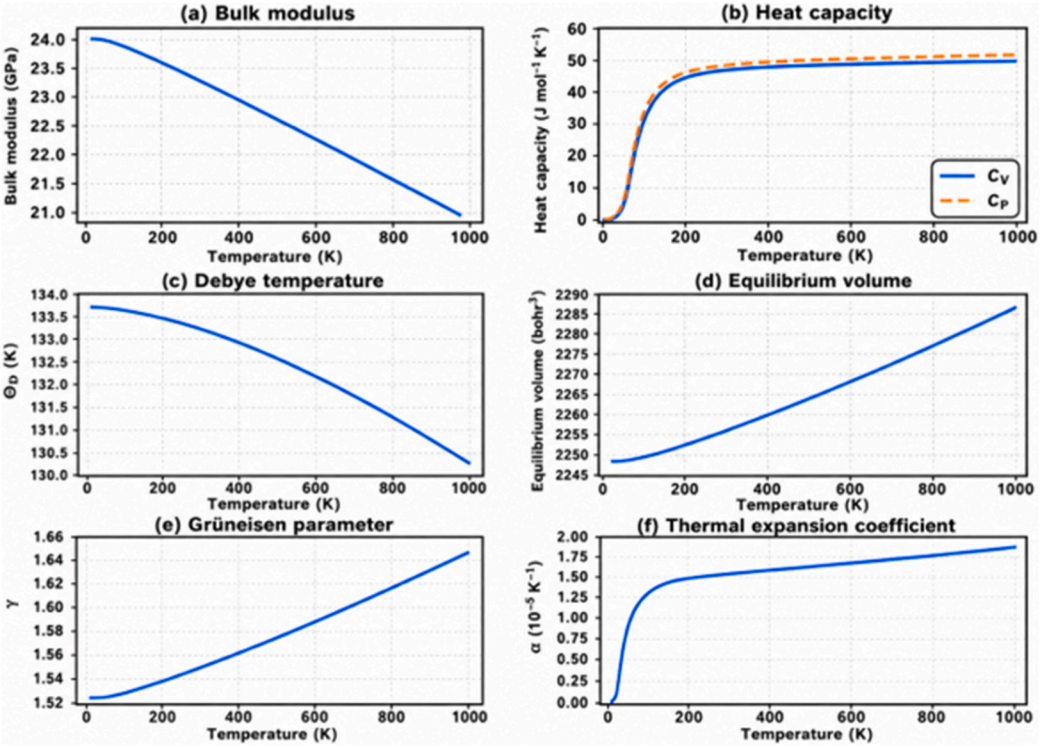


Fig. 9. Quasi-harmonic thermodynamic properties of Cs_2KGaCl_6: (a) bulk modulus, (b) Cp and Cv, (c) Debye temperature, (d) equilibrium volume, (e) Grüneisen parameter, and (f) thermal expansion coefficient.

Table 5
Numerical inputs used to reproduce the Slack-model screening estimate. Temperature-dependent entries are reported at representative temperatures from the same quasi-harmonic dataset plotted in Fig. 9.

Input	300 K	600 K	900 K	Use in Slack model
Average atomic mass, $\overline{M}$ (u/atom)	58.733	58.733	58.733	composition
Primitive-cell atom count, n	10	10	10	Cs_2KGaCl_6 formula unit
Debye temperature, ΘD (K)	216.86	204.47	188.63	quasi-harmonic output
Grüneisen parameter, γ	1.7393354	1.8278033	1.9660270	quasi-harmonic output
Primitive-cell volume (bohr^3)	2311.9017	2389.4523	2493.3932	quasi-harmonic output
Atomic volume, δ^3 (Å^3/atom)	34.2588	35.4080	36.9483	V/n
Temperature, T (K)	300	600	900	explicit Slack denominator
Slack-estimated κL (W m^{-1} K^{-1})	0.014698	0.005614	0.002564	Debye–Grüneisen scaling estimate

indicating progressive weakening of the restoring forces. Cp and Cv rise rapidly at low temperature and approach their high-temperature regime as vibrational modes become populated. The Debye temperature follows the evolving stiffness, whereas the Grüneisen parameter and thermal-expansion coefficient reflect increasing anharmonicity. These trends extend the zero-temperature softness inferred from the GGA equation of state into the thermal domain. The practical importance of thermal control for photoelectronic performance is also illustrated by recent photovoltaic thermal-management studies [52], although the present work addresses intrinsic lattice trends rather than device cooling.

3.7. Mechanical and phonon stability

Geometric screening and direct lattice-dynamical calculations provide complementary checks on the cubic structure. Using Shannon radii Cs^+(XII) = 1.88 Å, K^+(VI) = 1.38 Å, Ga^{3+}(VI) = 0.62 Å and Cl^-(VI) = 1.81 Å gives a Goldschmidt-type tolerance factor t = 0.929 and an octahedral factor μ = 0.552. These geometric factors are used only as screening descriptors; the stability assessment is based primarily on elastic and phonon calculations. The final elastic calculation was repeated using a denser 3000-k-point sampling. The resulting cubic elastic constants are C_{11} = 18.546 GPa, C_{12} = 18.539 GPa and C_{44} = 19.998 GPa. The Born requirements $C_{11}-C_{12} > 0$, $C_{11}+2C_{12} > 0$ and $C_{44} > 0$ are satisfied, with $C_{11}-C_{12}$ = +0.007 GPa. The small positive tetragonal-shear difference indicates a very soft elastic channel close to the mechanical-stability boundary. Recent first-principles work on Ga-based Cs_2NaGaX_6 double perovskites likewise highlights the strong sensitivity of mechanical response to halogen coordination [42]. Dynamical stability was assessed independently by finite-displacement phonon calculations using a 2 × 2 × 2 supercell. The phonon dispersion in Fig. 10 contains no imaginary branches along the sampled high-symmetry path. Thus, the present results support dynamical stability of the investigated cubic phase. The geometric, elastic, and dynamical-stability descriptors are summarized in Table 6.

This conclusion is distinct from hydrostatic equilibrium inferred from E(V), and it does not constitute a formation-energy or convex-hull proof of thermodynamic stability relative to competing phases.A closely related stability strategy has been applied to Cs_2AgBiX_6 (X = Br, Cl), where elastic constants/Born criteria were combined with phonon dispersions and finite-temperature thermodynamic descriptors to distinguish mechanical, dynamical and thermal stability. The same hierarchy is adopted here: the E(V) minimum establishes hydrostatic equilibrium, the elastic constants test mechanical stability, and the 2 × 2 × 2 phonon calculation provides the direct dynamical-stability check. Directional

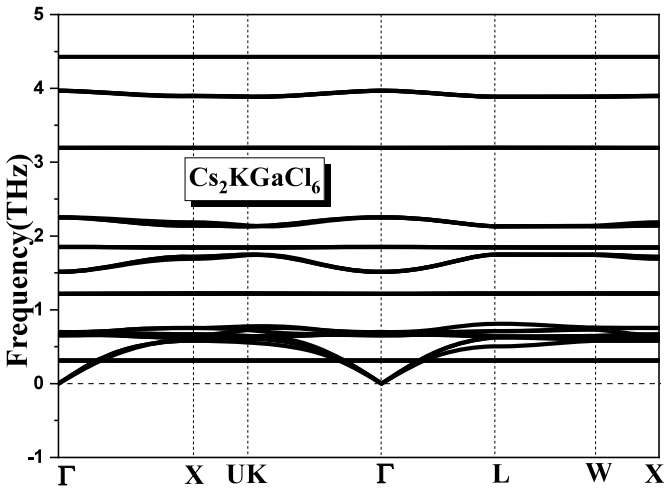


Fig. 10. Phonon dispersion and total phonon density of states of cubic Cs_2KGaCl_6 calculated with a 2 × 2 × 2 finite-displacement supercell. No imaginary phonon branches are observed.

Table 6
Geometric, elastic and dynamical-stability descriptors of cubic Cs_2KGaCl_6.

Descriptor	Value	Interpretation
Tolerance factor, t	0.929	Geometric screening
Octahedral factor, μ	0.552	Geometric screening
C_{11}	18.546 GPa	Elastic constant
C_{12}	18.539 GPa	Elastic constant
C_{44}	19.998 GPa	Elastic constant
$C_{11}-C_{12}$	+0.007 GPa	Positive; very soft tetragonal shear
$C_{11}+2C_{12}$	55.624 GPa	Positive
Born criteria	Satisfied	Mechanically stable cubic phase
Phonon supercell	2 × 2 × 2	Finite-displacement calculation
Imaginary phonon branches	None observed	Dynamically stable on sampled path
E[100]	0.0105 GPa	Minimum directional Young modulus
E[110]	0.0420 GPa	Intermediate cubic direction
E[111]	44.13 GPa	Maximum directional Young modulus
Emax/Emin	≈4.2 × 10^3	Extreme elastic anisotropy; ELATE formalism [53]

elasticity was re-evaluated using the compliance-tensor formalism implemented by ELATE [53]. The resulting values are E[100] = 0.0105 GPa, E[110] = 0.0420 GPa and E[111] = 44.13 GPa, corresponding to an extreme Emax/Emin ratio of about 4.2 × 10^3. This very large anisotropy is a direct consequence of the converged but exceptionally small positive $C_{11}-C_{12}$ = 0.007 GPa; it therefore reinforces, rather than hides, the conclusion that the cubic phase lies very close to the tetragonal-shear stability boundary.

The present results can also be placed in the context of earlier and recent first-principles work by Ghebouli and co-workers. For lead-free Cs_2AgBiX_6 (X = Br, Cl), structural, elastic, electronic and optical calculations established a useful halide-double-perovskite benchmark [54]. More recently, an integrated WIEN2k study of (Cs_2, K_2, Rb_2)$PbCl_6$ combined mechanical and dynamical stability with mBJ electronic, optical and thermoelectric analyses [55], while the related (Cs_2, K_2, Rb_2)$SnCl_6$ series demonstrated how B-site chemistry modifies the stability, band structure and thermoelectric response of cubic chloride double perovskites [56]. These studies provide a consistent comparative framework for interpreting the coupled elastic, optoelectronic and transport behavior obtained here for Cs_2KGaCl_6.Three-dimensional representation of the directional Young's modulus anisotropy of Cs_2KGaCl_6, reconstructed from the converged cubic elastic tensor using the ELATE compliance-tensor formalism [53]. Due to the exceptionally large anisotropy ratio (E[111]/E[100] > 4 × 10^3), logarithmic radial scaling is applied solely for visualization, while the color bar reports the actual Young's modulus values in GPa(Fig. 11). The pronounced anisotropy arises from the very small but positive $C_{11} - C_{12}$ value, indicating that Cs_2KGaCl_6 lies close to the tetragonal-shear mechanical stability limit.

Experimental outlook. A realistic synthesis route would start from dry, high-purity CsCl, KCl and $GaCl_3$ in the nominal 2:1:1 stoichiometry, followed by intimate mixing under an inert/dry atmosphere and sealed-tube or covered-crucible solid-state reaction with staged annealing. Solution-assisted crystallization from chloride-rich media is another plausible route if Ga^{3+} hydrolysis is rigorously suppressed. The principal challenges are the hygroscopic/volatile character of $GaCl_3$, moisture sensitivity, possible chloride loss at elevated temperature, antisite disorder on the K/Ga sublattices, and competition with binary/ternary chlorides. Phase-pure synthesis should therefore be verified by powder XRD/Rietveld refinement, composition analysis, and temperature-dependent diffraction before comparing optical or transport measurements with the present ideal-crystal predictions. A complete global interchange of the crystallographic 4a and 4b B-site labels in the ideal Fm-3m cell is related to an origin/sublattice relabeling of the ordered rock-salt B/B′ framework and does not by itself define an independent antisite defect energy. A physically meaningful K↔Gaantisite comparison requires a supercell containing a local exchanged K–Ga pair and full relaxation; such a defect calculation is beyond the pristine-cell scope of the present study. We have clarified this distinction to avoid reporting an artificial 'different-position' total-energy difference for symmetry-related ideal descriptions.

4. Conclusions

This work develops a complete all-electron description of Cs_2KGaCl_6 by linking structural energetics, corrected band dispersion, dielectric/optical behavior, carrier transport and lattice thermodynamics. LDA and GGA-PBE locate clear internal minima and reveal the expected expansion/softening relation, establishing a stable hydrostatic reference for the remaining calculations. The scalar-relativistic electronic result is a direct wide-gap semiconductor: Eg increases from 3.033 eV in GGA-PBE to 4.905 eV with TB-mBJ. Reliable GGA/TB-mBJ masses consistently show lighter electrons than holes. The optical response follows the corrected electronic structure. Static $\varepsilon_1(0)$ and n(0) decrease after TB-mBJ, the absorption edge shifts toward higher photon energy, and the refractive/loss spectra identify a wide-gap short-wavelength response rather than a low-energy metallic one. These features make Cs_2KGaCl_6 more naturally relevant to UV/near-UV optoelectronics, optical filtering or transparent functional layers than to a conventional narrow-gap solar absorber. Boltzmann transport shows useful Seebeck coefficients and finite power-factor maxima on both carrier branches, but their optimal chemical potentials move with temperature. The Slack lattice conductivity decreases with T and is qualitatively consistent with the soft lattice, although its absolute magnitude remains model sensitive. Experimental optical-gap measurements, temperature-dependent Seebeck/conductivity data and direct thermal-conductivity measurements would provide the most decisive validation. Additional validation completed in the revised analysis resolves the SOC caveat stated above: the independently checked TB-mBJ + SOC band structure is direct at Γ with Eg = 4.881 eV, compared with 4.905 eV without SOC. The 2 × 2 × 2 phonon spectrum contains no imaginary branches, and the dense-k elastic constants satisfy the cubic Born criteria. The optical spectra are interpreted within the independent-particle approximation, while explicit excitonic effects are not included. The absolute ZT and Slack κL values remain screening-level quantities because of the assumed relaxation time and Debye/Slack approximations. The geometric tolerance/octahedral-factor screening, phonon calculation and elastic analysis consistently support the investigated cubic configuration. The lower electron effective mass is therefore interpreted only as suggesting a potentially more favorable band-transport response under comparable scattering rates. The wide-gap UV/near-UV response and thermoelectric

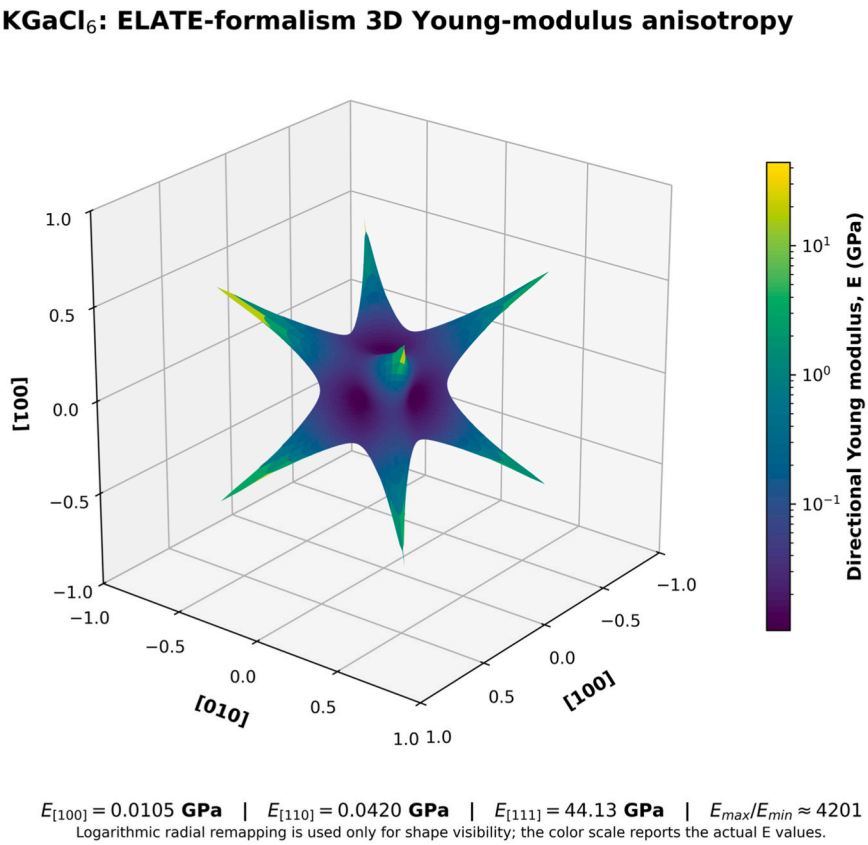


Fig. 11. Three-dimensional directional Young-modulus anisotropy of Cs_2KGaCl_6 reconstructed from the converged cubic elastic tensor using the ELATE compliance-tensor formalism.

screening correspond to distinct application regimes and would require different carrier-control strategies. The verified SOC result replaces the earlier anomalous post-processing value in the quantitative discussion. Mechanical and phonon stability are now demonstrated directly, whereas formation-energy/convex-hull stability, explicit phonon lifetimes and finite-temperature AIMD are not claimed beyond the calculations actually performed. The TB-mBJ + SOC calculations yield a direct Γ→Γ band gap of 4.881 eV, indicating that spin–orbit coupling produces only a modest reduction in the band gap relative to the scalar-relativistic TB-mBJ value. This result confirms the preservation of the wide-gap semiconducting character of Cs_2KGaCl_6 upon inclusion of relativistic effects and is therefore used in the subsequent analysis of its electronic properties.

CRediT authorship contribution statement

Zina Saoudi: Investigation. **M.A. Ghebouli:** Formal analysis. **M. Fatmi:** Writing – original draft, Validation. **Murat Yaylacı:** Writing – review & editing. **Elkenany Brens Elkenany:** Software. **Rashed Abu Hammour:** Methodology. **Ramzi Dhahri:** Formal analysis. **Giovanni Neri:** Methodology.

Funding

This work was funded by the Deanship of Graduate Studies and Scientific Research at Najran University under the Elite Funding Program, grant code NU/EP/SERC/14/4224-1.

Declaration of competing interest

The authors declare that they have no known competing financial interests or personal relationships that could have appeared to influence the work reported in this paper.

Acknowledgment

The authors are thankful to the Deanship of Graduate Studies and Scientific Research at Najran University for funding this work under the Elite Funding Program grant code (NU/EP/SERC/14/4224-1).

Data availability

No data was used for the research described in the article.

References

[1] S. Ghosh, H. Shankar, P. Kar, Recent developments of lead-free halide double perovskites: a new superstar in the optoelectronic field, Mater. Adv. 3 (2022) 3742–3765.
[2] H. Bendjilali, S. Rabhi, A.I. Shimul, S. Sadaf, S.A. Ansari, M.W. Alam, Uncovering a stable $Cs_2SnGeCl_6$ lead-free halide double perovskite for photovoltaics through integrated DFT and SCAPS-1D analysis, RSC Adv. 16 (2026) 22006–22020, https://doi.org/10.1039/D6RA01612J.
[3] S.M.K.A. Naqvi, S. Abdalla, K. Akhtar, A. Ali, N.Y. Elamin, F. Abbas, A.M. Khan, R. A. Khera, Exploring lead-free Rb_2AlInX_6 halide double perovskites for advanced energy-harvesting applications, RSC Adv. 15 (2025) 44116–44124, https://doi.org/10.1039/D5RA06712J.
[4] F. Ali, M. Hussain, H. Ullah, J.-T. Wang, M. Alomar, Optoelectronic and thermoelectric response of lead-free halide double perovskites Rb_2BiAuX_6 (X = Cl, Br, I) for energy-storage applications, RSC Adv. 15 (2025) 37999–38013.
[5] S. Wang, H. Li, L. Qi, K. Pan, Lead-free halide double-perovskite nanocrystals: structure, synthesis, optoelectronic properties, and applications, J. Mater. Chem. C 13 (2025) 19080–19105, https://doi.org/10.1039/D5TC02430G.
[6] D.Y. Heo, M.A. Tekalgne, S.Y. Kim, Research progress and perspectives on photocatalysts based on the lead-free double halide perovskite, EES Catal. 2 (2024) 94–108, https://doi.org/10.1039/D3EY00229B.
[7] R. Rafiu, I.A. Apon, M.A. Rahman, A.M. Alsuhaibani, M.S. Refat, M. Benghanem, S. AlFaify, N. Elboughdiri, Theoretical investigation of Rb-based double halide perovskites for photovoltaic, photocatalytic water-splitting, and CO_2 reduction

applications, RSC Adv. 16 (2026) 30158–30179, https://doi.org/10.1039/D6RA02841A.
[8] S.K. Fatima, R.H. Alzard, R. Amna, M.H. Alzard, K. Zheng, M. Abdellah, Lead-free perovskites for next-generation applications: a comprehensive computational and data-driven review, Mater. Adv. 6 (2025) 7634–7661, https://doi.org/10.1039/D5MA00681C.
[9] S.D. Dipta, J. Islam, S. Gouadria, M.S. Ahmad, A. El-Rayyes, M. Saiduzzaman, First-principles investigation of lead-free double perovskites Cs_2NaGaX_6 (X = F, Cl, br) for optoelectronic applications, New J. Chem. 50 (2026) 4910–4928, https://doi.org/10.1039/D5NJ04533A.
[10] H.A. Alburaih, G.M. Mustafa, P.A. Nawaz, S. Saba, N.A. Noor, A. Mahmood, R. Sharma, First principles investigation of halide based Rb_2NaGaZ_6 (Z = Br, I) double perovskites for energy harvesting applications, RSC Adv. 13 (2023) 35799–35809, https://doi.org/10.1039/D3RA05060B.
[11] M.A. Rehman, O. Manzoor, Z. ur Rehman, A.A. Ifseisi, J. Fatima, M. Usman, A. Farid, A. Hamad, Study of physical properties of Cs_2TlGaX_6 (X = Cl, Br) halide perovskites via HSE-06 hybrid technique for high efficiency solar cells, Opt. Quant. Electron. 56 (2024) 1079, https://doi.org/10.1007/s11082-024-07038-7.
[12] F. Ji, J. Klarbring, F. Wang, W. Ning, L. Wang, C. Yin, J.S.M. Figueroa, C. K. Christensen, M. Etter, T. Ederth, L. Sun, S.I. Simak, I.A. Abrikosov, F. Gao, Lead-free halide double perovskite $Cs_2AgBiBr_6$ with decreased band gap, Angew. Chem. Int. Ed. 59 (2020) 15191–15194, https://doi.org/10.1002/anie.202005568.
[13] C.J. Bartel, C. Sutton, B.R. Goldsmith, R. Ouyang, C.B. Musgrave, L.M. Ghiringhelli, M. Scheffler, New tolerance factor to predict the stability of perovskite oxides and halides, Sci. Adv. 5 (2019) eaav0693.
[14] J.P. Perdew, K. Burke, M. Ernzerhof, Generalized gradient approximation made simple, Phys. Rev. Lett. 77 (1996) 3865–3868.
[15] F. Tran, P. Blaha, Accurate band gaps of semiconductors and insulators with a semilocal exchange–correlation potential, Phys. Rev. Lett. 102 (2009) 226401.
[16] F. Tran, P. Blaha, Merits and limits of the modified becke–johnson exchange potential, Phys. Rev. B 83 (2011) 195134.
[17] D. Koller, F. Tran, P. Blaha, Improving the modified becke–johnson exchange potential, Phys. Rev. B 85 (2012) 155109.
[18] H. Jiang, Band gaps from the tran–blaha modified becke–johnson approach: a systematic investigation, J. Chem. Phys. 138 (2013) 134115.
[19] J. Even, L. Pedesseau, J.-M. Jancu, C. Katan, Importance of spin–orbit coupling in hybrid organic/inorganic perovskites for photovoltaic applications, J. Phys. Chem. Lett. 4 (2013) 2999–3005.
[20] F.P. Sabino, X.G. Zhao, G.M. Dalpian, A. Zunger, Impact of symmetry breaking and spin–orbit coupling on the band gap of halide perovskites, Phys. Rev. B 110 (2024) 035160, https://doi.org/10.1103/PhysRevB.110.035160.
[21] P. Blaha, K. Schwarz, P. Sorantin, S.B. Trickey, Full-potential, linearized augmented plane wave programs for crystalline systems, Comput. Phys. Commun. 59 (1990) 399–415.
[22] P. Blaha, K. Schwarz, G.K.H. Madsen, D. Kvasnicka, J. Luitz, R. Laskowski, F. Tran, L.D. Marks, WIEN2k: an Apw+Lo Program for Calculating Crystal Properties, Technische Universität Wien, Austria, 2001–2019.
[23] M.A. Blanco, E. Francisco, V. Luaña, GIBBS: Isothermal–Isobaric thermodynamics of solids from energy curves using a quasi-harmonic debye model, Comput. Phys. Commun. 158 (2004) 57–72.
[24] A. Otero-de-la-Roza, V. Luaña, Gibbs2: a new version of the quasi-harmonic model code. I. robust treatment of the static data, Comput. Phys. Commun. 182 (2011) 1708–1720.
[25] A. Otero-de-la-Roza, D. Abbasi-Pérez, V. Luaña, Gibbs2: a new version of the quasi-harmonic model code. II. Models for solid-state thermodynamics, features and implementation, Comput. Phys. Commun. 182 (2011) 2232–2248.
[26] C. Toher, J.J. Plata, O. Levy, M. de Jong, M. Asta, M.B. Nardelli, S. Curtarolo, High-throughput computational screening of thermal conductivity, Debye temperature, and grüneisen parameter using a quasiharmonic Debye model, Phys. Rev. B 90 (2014) 174107.
[27] G.K.H. Madsen, D.J. Singh, BoltzTraP. A code for calculating band-structure dependent quantities, Comput. Phys. Commun. 175 (2006) 67–71, https://doi.org/10.1016/j.cpc.2006.03.007.
[28] G.K.H. Madsen, J. Carrete, M.J. Verstraete, BoltzTraP2, a program for interpolating band structures and calculating semi-classical transport coefficients, Comput. Phys. Commun. 231 (2018) 140–145, https://doi.org/10.1016/j.cpc.2018.05.010.
[29] F. Birch, Finite elastic strain of cubic crystals, Phys. Rev. 71 (1947) 809–824.
[30] F.D. Murnaghan, The compressibility of media under extreme pressures, Proc. Natl. Acad. Sci. USA 30 (1944) 244–247.
[31] K. Bouferrache, M.A. Ghebouli, M. Fatmi, F.K. Alanazi, S. Saidi, S. Alomairy, A. Smerat, M. Yaylacı, Sustainable lead-free Na_2AgSbX_6 (X = Cl, F) double perovskites with tunable optoelectronic and thermoelectric properties: a first-principles study, Mater. Today Adv. 31 (2026) 100872, https://doi.org/10.1016/j.mtadv.2026.100872.
[32] K. Bouferrache, M.A. Ghebouli, M. Fatmi, F.K. Alanazi, S. Saidi, T.M. Althagafi, A. Smerat, M. Yaylacı, First-principles investigation of optical and plasmonic response of lead-free Rb_2AgSbX_6 (X = Br, I) double perovskites, Plasmonics 21 (2026) 2765–2781, https://doi.org/10.1007/s11468-026-03396-y.
[33] K. Bouferrache, M.A. Ghebouli, M. Fatmi, A.M. Saeedi, S. Alomairy, M.J. A. Abualreish, A. Smerat, First-principles study of band gap engineering and thermoelectric performance in K_2AgSbX_6 (X = Cl, F, I) double perovskites, Sci. Rep. 16 (2026) 26803, https://doi.org/10.1038/s41598-026-58427-9.
[34] K. Bouferrache, M.A. Ghebouli, M. Fatmi, B. Ghebouli, S. Alomairy, A. Omri, Analysis of the structural, electronic, and thermoelectric properties of lead-free Cs_2AgBiX_6 (X = Br, cl) double perovskites for non-toxic technologies, Phys. Mesomech. 29 (2026) 515–524, https://doi.org/10.1134/S1029959925600648.
[35] K. Bouferrache, M.A. Ghebouli, M. Fatmi, G. Sheetah, S. Alomairy, M.J. A. Abualreish, A. Smerat, M. Yaylacı, Synergistic optoelectronic and thermoelectric performance in $Rb_2AsAuBr_6$ and $Rb_2AsAuCl_6$ double perovskites for multifunctional energy conversion, Sci. Rep. 16 (2026) 13616, https://doi.org/10.1038/s41598-026-42440-z.
[36] F. Benlakhdar, M.A. Ghebouli, M. Fatmi, B. Ghebouli, S. Alomairy, M.J. A. Abualreish, T. Althagafi, W. Djerir, Electronic and optical properties of lead-free $K_2AgSbBr_6$ double perovskite tuned by doping elements cu^+, Bi^{3+}, and I^-, Sci. Rep. 15 (2025) 40362, https://doi.org/10.1038/s41598-025-24417-6.
[37] M. Fatmi, K. Bouferrache, M.A. Ghebouli, B. Ghebouli, F.K. Alanazi, M. D. Albaqami, S. Mohammad, A. Benali, High performance double perovskites of $Cs_2InAgBr_6$ and $Cs_2InAgCl_6$ structural electronic optical and thermoelectric properties for next generation photovoltaics, Sci. Rep. 15 (2025) 20851, https://doi.org/10.1038/s41598-025-04600-5.
[38] N.K. Singh, A. Kumar, S. Kumar, V.K. Nautiyal, R. Kumar, A. Kumar, N. Iram, A comprehensive theoretical analysis of Cs_2KGaX_6 (X = Cl, Br, I): for green energy solutions, Solid State Commun. 401 (2025) 115929, https://doi.org/10.1016/j.ssc.2025.115929.
[39] A. Usman, A. Ayyaz, Q. Mahmood, N. Algethami, S.A. Mahmoud, I. Boukhris, A. K. Alqorashi, Investigation of structural, optoelectronic, and transport properties of A_2AuSbZ_6 (A = Na, K; Z = F, cl) double perovskites for energy conversion applications, J. Korean Ceram. Soc. 62 (2025) 526–538, https://doi.org/10.1007/s43207-025-00483-4.
[40] Z. Benneghmouche, T. Melki, K. Bouferrache, M. Fatmi, F.K. Alanazi, S. Alomairy, M. Alotaibi, A. Smerat, Unveiling the structural, electronic, optical, and transport properties of Cs_2SeCl_6 double perovskite for clean energy, Sci. Rep. (2026), https://doi.org/10.1038/s41598-026-62677-y.
[41] X. An, X. Zhang, H. Zhang, Y. Liu, J. Chen, J. Shi, G. Shao, H. Xu, H. Wang, H. Lu, Visible light responsive high-entropy $Cs_2AgInCl_6$ double perovskite nanoparticles photocatalyst with high water resistance, Sep. Purif. Technol. 395 (2026) 137729, https://doi.org/10.1016/j.seppur.2026.137729.
[42] Y. Yin, H. Xu, J. Li, J. Zhao, S. Yang, R. Meng, G. Yuan, H. Ma, F. Li, Halogen-coordination-induced ductility enhancement transition and atomic-scale failure mechanisms in Ga-based double perovskites Cs_2NaGaX_6 (X = Cl, br): a first-principles study, Comput. Mater. Sci. 274 (2026) 115041, https://doi.org/10.1016/j.commatsci.2026.115041.
[43] M.Y. Khan, M.A. Jehangir, I.E. Lee, Q. Wali, T. Usman, M. Yang, A. Al Souwaileh, Thermodynamic, quantum efficiency, and photocatalytic properties of Cs_2MZ_6 (M = Ti, Zr, hf; Z = Cl, I) double perovskites using DFT approach, AIP Adv. 15 (2025), https://doi.org/10.1063/5.0293200.
[44] T. Usman, S. Khan, D.F. Khan, G. Murtaza, M.Y. Khan, Tailoring halide perovskite materials $CsTmX_3$ (X = F, Cl, Br, I) for enhanced optoelectronic and thermoelectric characteristics through first-principles investigations, Int. J. Mod. Phys. B 40 (2026) 2650088, https://doi.org/10.1142/S0217979226500888.
[45] T. Usman, J. Iqbal, M. Archi, M. Murtaza, S. Khan, Y. Mu, Tailoring halide double perovskite materials Rb_2MgSnY_6 (Y = I, Br, cl) for enhanced optoelectronic and solar cells through first-principles study, Opto-Electron. Rev. 33 (2025) e155902, https://doi.org/10.24425/opelre.2025.155902.
[46] M.A. Jehangir, M.Y. Khan, M. Noman, I.E. Lee, Q. Wali, T. Usman, Y. Mu, A. Al Souwaileh, First-principles investigation of lead-free Rb_3SbX_6 (X = F, Cl, Br, I) mixed-halide double perovskites promising for photovoltaics and scintillation, RSC Adv. 15 (2025) 33708–33725, https://doi.org/10.1039/D5RA04902D.
[47] T. Usman, J. Iqbal, S. Ullah, M.Y. Khan, S.A. Khan, M. Hanif, G.-R. Yao, First-principles investigation of structural stability and optoelectronic properties of lead-free $A_2LiGaBr_6$ (A = Na, K) double perovskites for photovoltaic applications, Polyhedron 296 (2026) 118218, https://doi.org/10.1016/j.poly.2026.118218.
[48] Q. Mahmood, T. Zelai, T. Usman, S. Al-Qaisi, M. Morsi, H. Albalawi, A.I. Aljameel, O.A. Alamri, G. Murtaza, First-principles study of lead-free double perovskites $K_2Pt(Cl/Br)_6$ for optoelectronic and renewable energy applications, J. Solid State Chem. 301 (2021) 122294, https://doi.org/10.1016/j.jssc.2021.122294.
[49] T. Usman, J. Iqbal, M. Hanif, M. Archi, M.Y. Khan, S. Ullah, G.-R. Yao, S.A. Khan, Prospecting K_2InLiX_6 (X = Cl, Br, I) double perovskite for photovoltaic and optoelectronic applications: a DFT-Based analysis, Chem. Pap. 80 (2026) 12119–12130, https://doi.org/10.1007/s11696-026-05120-w.
[50] M.E.A. Monir, H. Baltach, K. Bouferrache, M. Fatmi, M.A. Ghebouli, F.K. Alanazi, B. Ghebouli, M.I. Benamrani, R. Boudissa, Half-metallicity of novel halide double perovskites K_2CuVCl_6 and Rb_2CuVCl_6: application in next-generation spintronic devices, RSC Adv. 15 (2025) 17685–17694, https://doi.org/10.1039/D5RA02811F.
[51] D.-A. Park, N.-G. Park, Perovskite-inspired materials (PIMs): exploring their potential for photovoltaic applications, SusMat 5 (2025) e70018, https://doi.org/10.1002/sus2.70018.
[52] G. Wang, Z. Zhang, Z. Chen, Experimental study on improving photoelectric performance of photovoltaic system by using potassium hydroxide-modified hydrogel, Appl. Therm. Eng. 303 (2026) 132283, https://doi.org/10.1016/j.applthermaleng.2026.132283.
[53] R. Gaillac, P. Pullumbi, F.-X. Coudert, ELATE: an open-source online application for analysis and visualization of elastic tensors, J. Phys. Condens. Matter 28 (2016) 275201, https://doi.org/10.1088/0953-8984/28/27/275201.
[54] M.A. Ghebouli, T. Chihi, B. Ghebouli, M. Fatmi, Study of the structural, elastic, electronic and optical properties of lead free halide double perovskites Cs_2AgBiX_6

(X = Br, cl), Chin. J. Phys. 56 (2018) 323–330, https://doi.org/10.1016/j.cjph.2018.01.004.

[55] M.A. Ghebouli, K. Bouferrache, F.K. Alanazi, B. Ghebouli, M. Fatmi, Computational insights into the stability, mechanical, optoelectronic, and thermoelectric characteristics investigation on lead-based double perovskites of (cs_2, K_2, Rb_2)$PbCl_6$: promising candidates for optoelectronic applications, Adv. Theory Simul. 8 (2025) 2400938, https://doi.org/10.1002/adts.202400938.

[56] M.A. Ghebouli, K. Bouferrache, F.K. Alanazi, B. Ghebouli, M. Fatmi, Stability, mechanical, optoelectronic and thermoelectric behaviors of inorganic metal halide double perovskites (cs_2, K_2, Rb_2)$SnCl_6$: promising green energy alternatives, Solid State Commun. 397 (2025) 115831, https://doi.org/10.1016/j.ssc.2025.115831.